

<https://doi.org/10.1038/s41612-024-00742-x>

Interdecadal shifts of ENSO influences on Spring Central Asian precipitation

Mengyuan Yao^{1,2,3}, Haosu Tang^{1,4}✉, Gang Huang^{1,2,3}✉ & Renguang Wu^{1,5}

Spring Central Asian precipitation (SCAP) holds significant implications for local agriculture and ecosystems, with its variability mainly modulated by El Niño–Southern Oscillation (ENSO). The ENSO–SCAP relationship has experienced pronounced interdecadal shifts, though mechanisms remain elusive. Based on observations and climate model simulations, these shifts may result from transitions in ENSO-induced meridional circulation and Rossby wave trains triggered by North Atlantic (NA) sea surface temperature (SST) anomalies. During high (low) correlation periods, ENSO induces strong (weak) vertical motion anomalies over Central Asia, while NA SST anomalies exert a weak (strong) counteracting effect, modulated by the Pacific decadal oscillation (PDO). In the positive (negative) phase of PDO, a slow (fast) decaying ENSO triggers a strong (weak) NA horseshoe-like SST anomaly in the post-ENSO spring, affecting the ENSO–SCAP relationship. Our study identifies a strengthening trend in the ENSO–SCAP relationship since the 2000s, indicating improved predictability for SCAP in recent decades.

Central Asia (CA), recognized as one of the largest semi-arid to arid regions in the world, includes Kazakhstan, Uzbekistan, Turkmenistan, Kyrgyzstan, and Tajikistan. This region features a typical continental climate and hosts a fragile ecosystem, particularly susceptible to changes in local precipitation. The primary rainy season in CA, especially in southern CA, is spring^{1,2}. The Spring Central Asian precipitation (SCAP) variability serves as a crucial indicator for local agricultural production, water sources, ecosystems, and economic activities. El Niño–Southern Oscillation (ENSO) is the dominant source of interannual variability in tropical ocean–atmosphere interactions. It exerts far-reaching impacts on global weather and climate via atmospheric teleconnections, and is a vital signal for seasonal forecasting and climate prediction worldwide^{3–5}. Numerous studies have demonstrated that ENSO exerts a significant impact on the precipitation variability in CA⁶, and spring precipitation over more than half of CA shows a positive correlation with El Niño in the preceding winter⁷. On the one hand, El Niño favors above-normal precipitation in CA as it enhances southwesterly water vapor flux from the Arabian Sea and tropical Africa, along with more northeasterly water vapor flux from Russia^{1,8}. This mechanism is confirmed by an atmospheric general circulation model experiment forced by observed sea surface temperatures (SST)^{1,6,8,9}. ENSO is also suggested to explain the large fluctuations of sea level pressure over the Caspian Sea¹⁰, which is an important moisture transport source for CA. On the other hand, El Niño could lead to upper-level divergence anomalies over CA through large-scale

convergence and divergence. This can induce anomalous updrafts, resulting in increased precipitation in the region^{11,12}. To sum up, El Niño (La Niña) typically leads to increased (decreased) precipitation over CA through enhanced (weakened) moisture transportation and intensified updrafts (downdrafts), though the spatial pattern of precipitation anomalies exhibits seasonal variations during different phases of ENSO¹³.

Changes in ENSO characteristics, such as flavors and intensity, contribute to diverse precipitation responses over CA. Previous studies have revealed that precipitation anomalies associated with cold-tongue El Niño mainly fall along the hills and Pamir Plateau, whereas those linked to warm-pool El Niño are concentrated around the mountains and the Aral area during the El Niño decaying spring⁸. Notably, the latter type of El Niño exerts a stronger influence on precipitation anomalies in CA. Regarding the varying intensity of El Niño events, stronger El Niño events normally lead to persisting above-normal precipitation over CA from the developing winter to decaying summer, whereas precipitation anomalies are less obvious in weaker El Niño events¹³.

Previous studies have indicated that North Atlantic (NA) SST anomalies play a crucial role in influencing Eurasian climate anomalies, serving as a source for predicting Eurasian climate variability. The positive phase of the NA horseshoe-like SST anomaly pattern could excite an atmospheric quasi-barotropic Rossby wave train extending from NA through Eurasia to downstream East Asia, leading to reduced

¹State Key Laboratory of Numerical Modeling for Atmospheric Sciences and Geophysical Fluid Dynamics (LASG), Institute of Atmospheric Physics, Chinese Academy of Sciences, Beijing, China. ²Laboratory for Regional Oceanography and Numerical Modeling, Qingdao National Laboratory for Marine Science and Technology, Qingdao, China. ³University of Chinese Academy of Sciences, Beijing, China. ⁴Department of Geography, University of Sheffield, Sheffield, UK. ⁵School of Earth Sciences, Zhejiang University, Hangzhou, China. ✉e-mail: tanghaosu@mail.iap.ac.cn; hg@mail.iap.ac.cn

rainfall east of the Caspian Sea and across CA^{14,15}. Besides, summer extreme precipitation in eastern CA shows a close correlation with NA SST anomalies as well¹⁶. It is worth mentioning that the horseshoe-like SST anomaly pattern over NA is tightly associated with the North Atlantic Oscillation (NAO), which strongly influences the precipitation over CA through upper-tropospheric westerly jets^{17–19}. Numerous researches have demonstrated that ENSO could induce the NA horseshoe-like SST anomaly pattern during its decaying spring. This is primarily attributed to surface heat flux anomalies resulting from the so-called atmospheric bridge (or teleconnection) induced by ENSO^{20,21}. It has also been pointed out that the positive phase of NA SST anomalies is more pronounced during spring in slow-decaying El Niño events compared to fast-decaying ones. This discrepancy can largely be attributed to differences in lower-level wind anomalies and the associated surface heat flux anomalies⁴. Thus, NA SST anomalies may act as an important bridge in the cross-seasonal impacts of ENSO on precipitation anomalies over CA.

Studies have been conducted in exploring the impacts of ENSO on SCAP, and emerging evidence implies that the relationship between ENSO and SCAP may not be consistently stable^{1,22}. However, the underlying mechanisms of interdecadal shifts remain a knowledge gap to date. In this study, we aim to investigate the plausible causes of interdecadal variations of the relationship between wintertime ENSO and subsequent SCAP. Given that relatively short observational records may constrain our understanding of interdecadal shifts, we also take advantage of climate model simulations from phase 6 of the Coupled Model Intercomparison Project (CMIP6). These simulations provide an extensive set of samples to verify the mechanisms driving interdecadal changes in the observations. By leveraging multiple observations and a subset of CMIP6 models capable of capturing interdecadal modulations, we discern the roles of Pacific and NA SST anomalies on the SCAP. We propose that the ENSO–SCAP relationship may be influenced by ENSO-induced large-scale meridional divergence and convergence, and zonal Rossby wave trains triggered by NA SST

anomalies. Idealized model simulations are also performed to validate the dynamic mechanisms.

Results

Interdecadal shifts of ENSO–SCAP relationship

Figure 1 depicts the regression and 19-year sliding correlation of precipitation over CA from the El Niño developing winter to decaying summer with normalized DJF(0) Niño3.4 index in the observations during 1891–2020. Seasonal precipitation features homogeneous wet anomalies across the whole of CA. From DJF(0) to JJA(1), the highest correlation persists in the southern and eastern parts of CA, while the lower correlation is sustained in the northern part. Precipitation anomalies also exhibit distinct seasonal differences, with wet anomalies intensifying and expanding to central CA from DJF(0) to MAM(1) and then weakening in JJA(1). Notably, precipitation anomalies are obviously larger during the El Niño decaying spring than in other seasons (Fig. 1a–c). The 19-year sliding correlations indicate pronounced interdecadal shifts, sharply declining in the 1930s and then gradually strengthening until the 1960s. Moreover, there is an increasing trend after the 2000s for DJF(0) and MAM(1). Hereafter, we focus on interdecadal shifts of ENSO influences on SCAP, given that spring is the major growing season for arid CA and precipitation variability during spring may hold the utmost significance. We further define the high correlation (HC) period and low correlation (LC) period based on the 19-year sliding correlation. Thus, the periods 1951–1969 and 1920–1938 are selected as the HC and LC periods in the observations, respectively. To ensure the reliability of our conclusions, we also calculate sliding correlations of SCAP with normalized DJF(0) Niño3.4 index using two additional window lengths and two other precipitation datasets. The results remain robust (Supplementary Fig. 1).

The regression and 19-year sliding correlation of SCAP with normalized DJF(0) Niño3.4 index in 45 CMIP6 models during 1891–2014 are shown in Supplementary Figs. 2 and 3, respectively. Most CMIP6 models could capture the unstable ENSO–SCAP relationship except for ACCESS-CM2, CESM2-WACCM, FGOALS-g3 and MIROC-ES2L (Supplementary Fig. 3). To investigate the

Fig. 1 | Response of different seasonal precipitation (unit: mm/day) to El Niño in observation. **a** Regression and **d** 19-year sliding correlation of the DJF(0) precipitation (based on GPCP) with the normalized DJF(0) Niño3.4 index in the observation for the period 1891–2020. **b**, **e** and **c**, **f** Same as (**a**, **d**), but for MAM(1) and JJA(1), respectively. The dots and dashed lines denote the 90% confidence level.

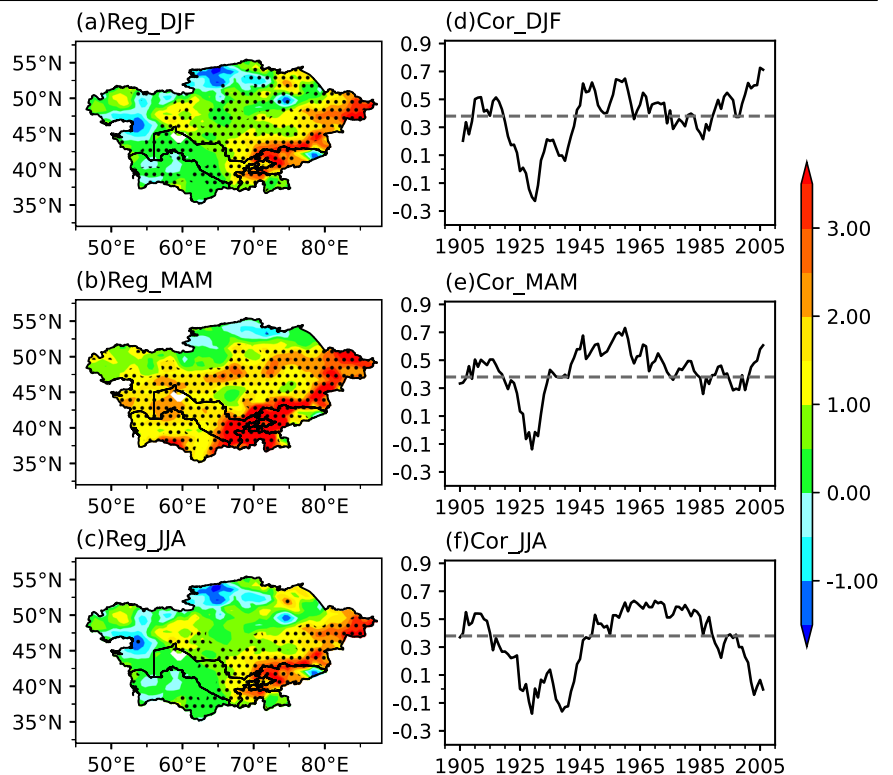
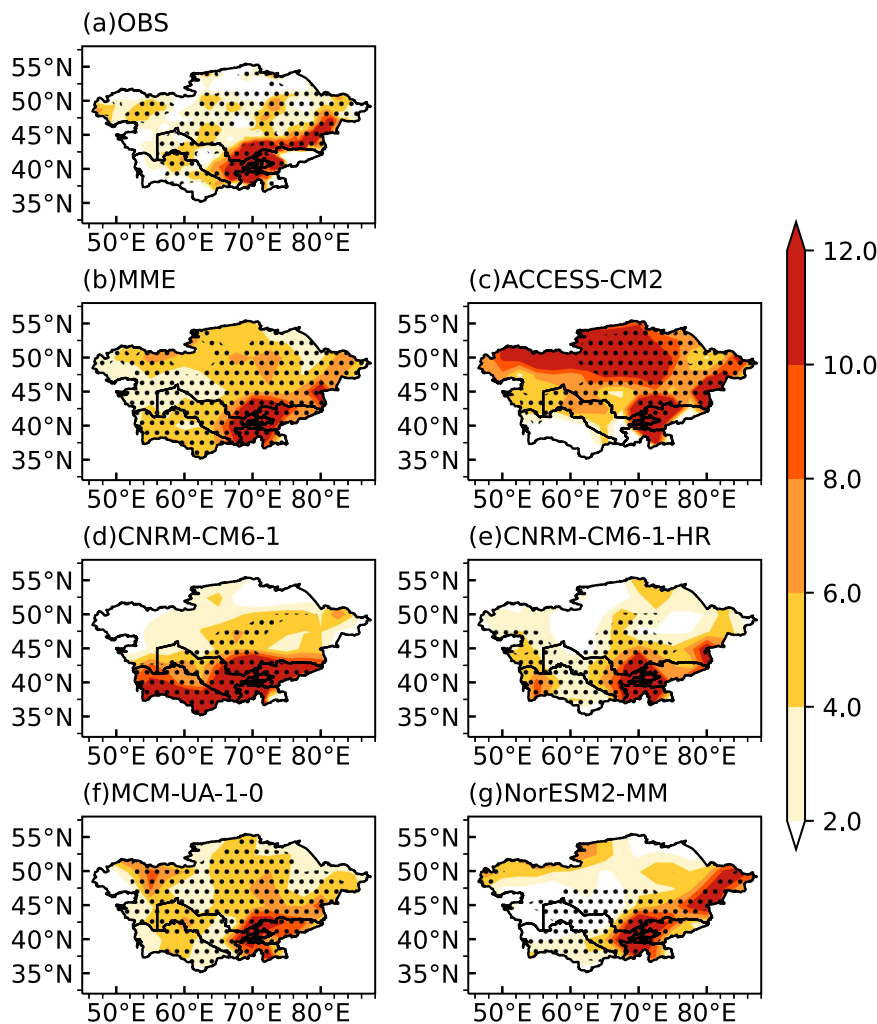


Fig. 2 | Response of precipitation (unit: mm/day) to El Niño in observation and selected models.

Regression of MAM(1) precipitation over CA with normalized DJF(0) Niño3.4 index for HC minus LC differences in **a** observation, **b** MME and **c–g** five selected models from CMIP6. From here on, MME is derived from five selected models. The dots denote the 90% confidence level in the observation and 80% consistency in models in the HC period.



physical mechanisms of the interdecadal variations, high-skill models are further selected. The criteria for selecting proper models involve ensuring a degree of fidelity in simulating the ENSO-related anomalous precipitation pattern over CA and the capability to reproduce the differences between HC and LC periods. Based on (a) the spatial correlation of ENSO-related precipitation anomalies over CA in each model with the observation during the whole period, (b) the spatial correlation during the HC period, and (c) the maximum minus minimum value of 19-year sliding correlation, five models are finally selected and the detailed results are listed in Supplementary Table 2. They are CNRM-CM6-1-HR, HadGEM3-GC31-LL, HadGEM3-GC31-MM, SAM0-UNICON, and UKESM1-0-LL, in which the spatial correlations with the observations are above 0.56 and 0.33 for the whole and HC period, respectively. And the difference in correlation values between HC and LC periods exceeds 0.77. Here, the definition of HC and LC periods in each model aligns with that in the observations. Note that lowering thresholds and incorporating additional models do not alter the conclusions of this study, as the results from CMIP6 models are mainly used for verification (figures not shown).

Can the selected five models accurately reproduce the spatial pattern of ENSO-induced precipitation anomalies over CA in MAM(1)? Figure 2 illustrates the difference in ENSO-induced SCAP anomalies between HC and LC periods. In the observations, enhanced precipitation tends to occur during the HC period, with the most significant positive values centered over southern and eastern CA. Despite slight differences in magnitude and location, the results from the multi-model ensemble mean (MME) and five

single models closely resemble the observed pattern. In other words, the models selected based on the above criteria can well capture the interdecadal changes in the relationship between ENSO and SCAP.

Potential mechanisms modulating the ENSO–SCAP relationship

Based on the observations and five models selected in the previous section, we explore the underlying mechanism for the interdecadal variations of the ENSO–SCAP relationship in this section.

Previous studies have suggested that ENSO influences the hydroclimate of CA through restructuring winds and moisture sources. Figure 3 shows the regression of MAM(1) vertically integrated moisture transportation and divergence with normalized DJF(0) Niño3.4 index in the observations and CMIP6 MME. During the HC period, notable cyclonic circulation anomalies are located over CA, with anomalous westerlies along the southern periphery favoring water vapor transport from the Atlantic and Mediterranean Sea in both observations and MME (Fig. 3a, c). As a result, moisture convergence anomalies are observed across nearly the entire region of CA, favoring above-normal local precipitation. In contrast, cyclonic circulation anomalies shift towards the west of CA during the observed LC period, while an anomalous anticyclonic circulation appears in northern CA (Fig. 3b). The northward moisture transport anomalies in southern CA carry moisture from the Indian Ocean to the region, although local moisture convergence anomalies are weaker compared to those in the HC period. Previous studies have found that during El Niño events, the weakened Pacific Walker circulation suppresses convection and precipitation over the Indo-western Pacific warm pool. This suppression induces a westward-propagating baroclinic Rossby wave train, leading to

Fig. 3 | Response of vertically integrated moisture transportation and its divergence to El Niño. Regression of MAM(1) vertically integrated moisture transportation (vectors; unit: kg/(m s)) and its divergence (colors; unit: 10^{-6} kg/s) with normalized DJF(0) Niño3.4 index for **a** HC period and **b** LC period in the observation. Green (brown) shadings denote moisture convergence (divergence) anomalies. **c, d** Same as **(a, b)**, but for MME.

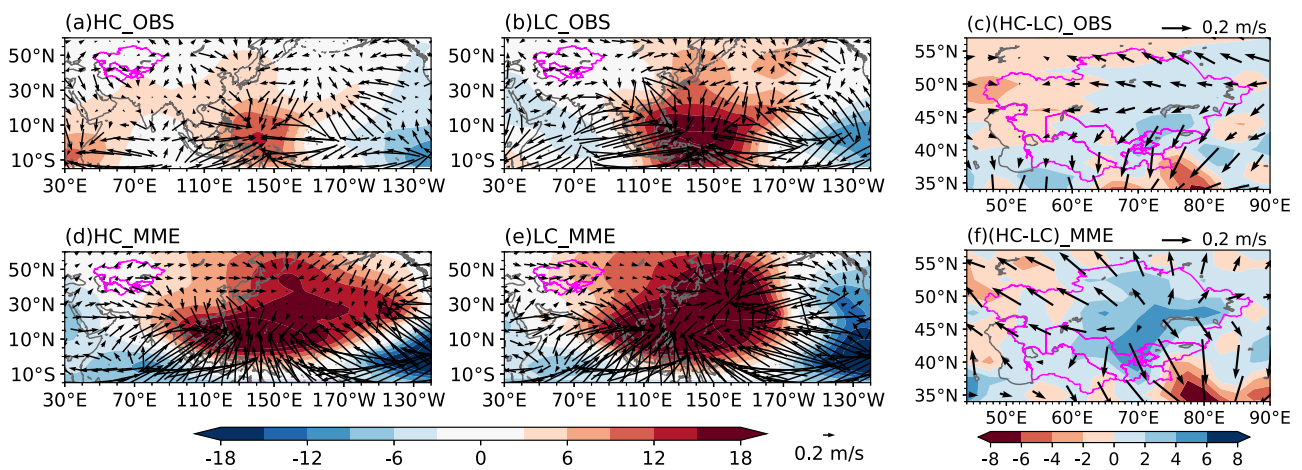
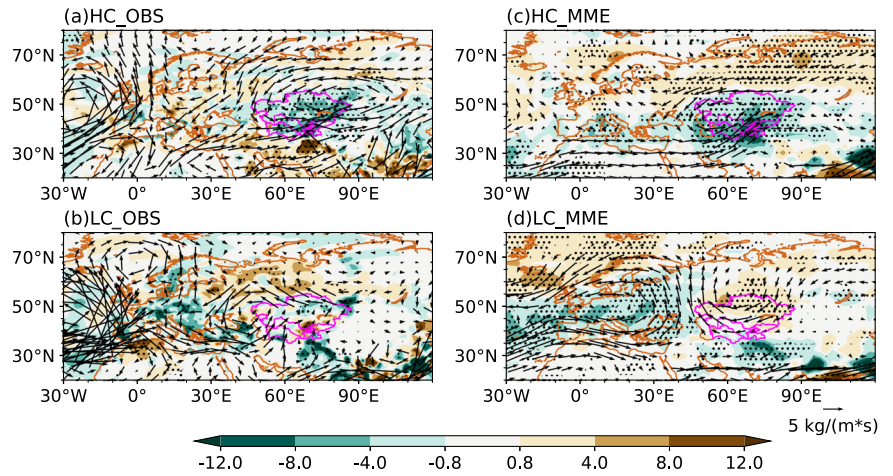


Fig. 4 | Response of 200-hPa velocity potential and divergent winds to El Niño. Regression of MAM(1) 200-hPa velocity potential (colors; 10^6 m²/s) and divergent winds (vectors; m/s) with normalized DJF(0) Niño3.4 index for **a** HC period and

b LC period in the observation. **c** Same as **(a)**, but for divergence (colors; 10^{-7} /s) and divergent winds (vectors; m/s) for HC minus LC differences. **d-f** Same as **a-c**, but for MME.

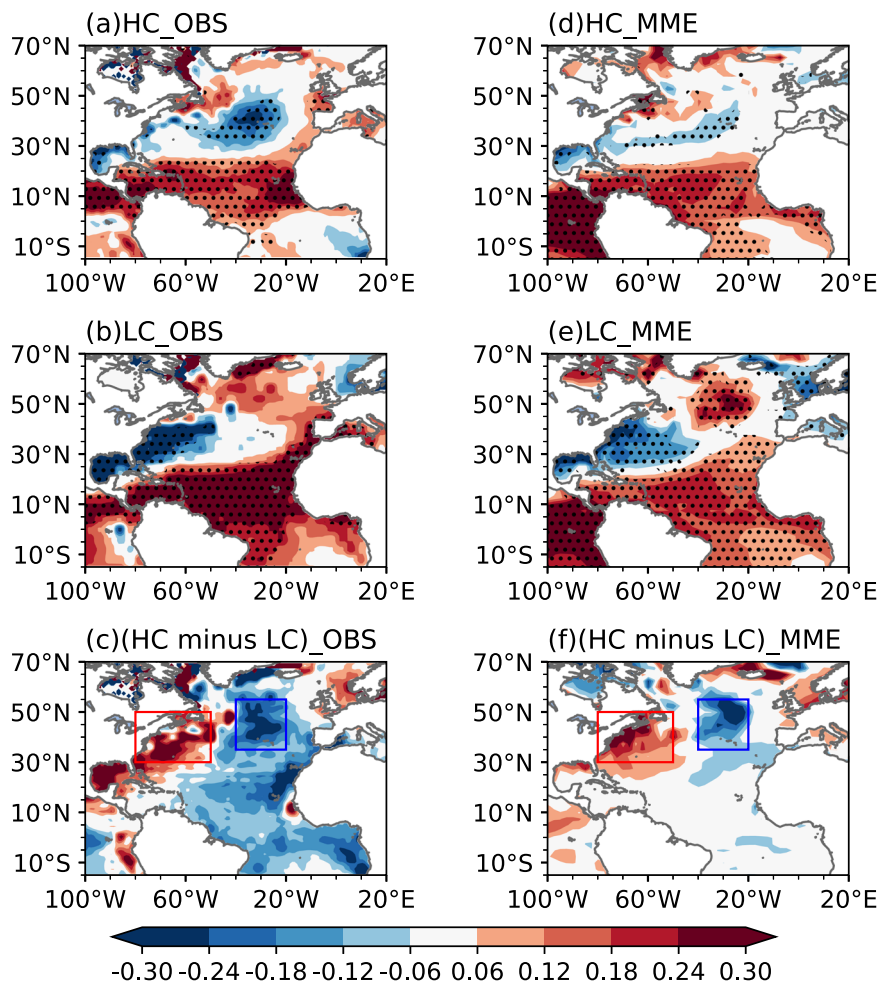
anticyclonic/high-pressure anomalies over the Indian Ocean and extending to southern CA. This process can explain enhanced southwesterly water vapor flux from the Indian Ocean to southern CA^{9,22-24}. MME results during the LC period display stronger anticyclonic circulation anomalies covering nearly the entire CA. This leads to easterly anomalies over northern CA, creating unfavorable conditions for water vapor transport from the oceans to reach the region (Fig. 3d). Consequently, moisture divergence anomalies occur, favoring below-normal precipitation across CA.

To further understand the ENSO-induced dynamic conditions over CA during the HC and LC periods, the regressions of MAM(1) 200-hPa velocity potentials and divergent winds against normalized DJF(0) Niño3.4 index in the observations and CMIP6 MME are shown in Fig. 4. The red (blue) colors indicate El Niño-induced upper-level convergence (divergence) anomalies. Notably, persistent upper-level convergence anomalies are evident over the western Pacific, while the anomalous upper-level divergence generally prevails over the eastern Pacific. Previous studies have indicated that ENSO could influence mid-latitude weather and climate via large-scale meridional convergence and divergence^{13,25,26}. During the HC period, CA is dominated by El Niño-induced upper-level divergence anomalies, which are conducive to anomalous ascent and increased precipitation across the region (Fig. 4a, d). Compared to the HC period, the upper-level divergence and divergent wind anomalies are weaker in the LC period in both observations and MME (Fig. 4c, f). Thus, both El Niño-induced anomalous

moisture transportation and ascending motion through large-scale convergence and divergence are stronger in the HC period compared to the LC period, which may account for the increased SCAP during the former period.

To further explore the potential mechanisms underlying the unstable relationship between ENSO and SCAP, the regressions of MAM(1) SST anomalies with normalized DJF(0) Niño3.4 index are examined for the HC and LC periods in the observations and CMIP6 MME (Fig. 5). A horseshoe-like SST anomaly pattern is salient in NA, characterized by cold SST anomalies near the east coast of the United States and warm SST anomalies in the NA subpolar gyre zone and tropical NA. Moreover, the horseshoe-like SST anomaly pattern is significantly stronger during the LC period than the HC period in both observations and MME (Fig. 5c, f). Compared to the observations, the difference in SST anomalies between the HC and LC periods over the tropical Atlantic is weaker in CMIP6 MME. Here, we construct an NA dipole SST index (NAI) to assess the impact of an NA horseshoe-like SST anomaly pattern on the SCAP. This index is defined as the difference between area-weighted regional mean SST anomalies over northeastern NA (blue box; 35°N–55°N, 20°W–40°W) and southwestern NA (red box; 30–50°N, 50–80°W). The regions are selected based on the anomalous SST difference between the HC and LC periods (Fig. 5c, f). The correlation between DJF(0) Niño3.4 index and MAM(1) NAI is insignificant during the

Fig. 5 | Response of Atlantic SST (unit: K) to El Niño. Regression of MAM(1) SST with normalized DJF(0) Niño3.4 index for **a** HC period, **b** LC period and **c** HC minus LC differences in the observation. **d–f** Same as **a–c**, but for MME. The dots denote the 90% confidence level in the observation and 80% consistency in models. The blue and red boxes denote the area of NA dipole SST index (40°W–20°W, 35°N–55°N) and (50°W–80°W, 30°N–50°N), respectively.



whole period in both observation and selected CMIP6 models, with correlation coefficients of 0.05 and 0.04 for the observation and CMIP6 MME, respectively.

Figure 6 illustrates the regression of MAM(1) 200-hPa geopotential height with normalized NAI and the corresponding wave activity flux in the observations and CMIP6 MME. The positive phase of the NA horseshoe-like SST anomaly pattern could trigger quasi-barotropic high-pressure anomalies across CA as part of the Eurasian Rossby wave train, thereby leading to decreased local precipitation (Supplementary Fig. 4). Figure 7 shows the 19-year sliding correlation of MAM(1) precipitation over CA and NAI against normalized DJF(0) Niño3.4 index in the observations and five selected models. In the observations, the sliding correlation between ENSO and NAI shows an upward trend before the 1930s and then gradually declines until the 1960s. Additionally, a decreasing trend is observed after the 1980s. The relationship between ENSO and NAI generally aligns well with the opposite evolution of the ENSO–SCAP relationship. Similar conclusions could be obtained in high-skill CMIP6 models as well. The 102-yr negative correlations between ENSO–NAI and ENSO–SCAP time series in the observations and simulations of each selected model can be further validated through a 99% significance test except for HadGEM3-GC31-MM. How to understand the dynamic processes behind the negative correlations? The results indicate that a stronger positive (negative) phase of the NA SST anomaly pattern corresponds to a weaker (stronger) relationship between El Niño and SCAP. During periods when the positive phase of the NA SST anomaly pattern is strong, it leads to an anticyclone occupying CA, suppressing local precipitation. This counteracts the direct wetting impacts of El Niño on SCAP, thereby resulting in a diminished ENSO–SCAP relationship. Conversely, the negative phase of the NA SST anomaly pattern induces

an anomalous cyclone located over CA, intensifying the wetting impacts caused by El Niño. This finally leads to an enhanced ENSO–SCAP relationship.

To validate whether the NA dipole SST anomalies could trigger the Eurasian teleconnection pattern, we further conducted three sets of linear baroclinic model (LBM) experiments. They are driven by positive vorticity forcing in northeastern NA, negative vorticity forcing in southwestern NA, and their sum, respectively, along with climatological mean flow during the boreal spring (Fig. 8a, c, and d). The prescribed vorticity source exhibits a cosine elliptical pattern, with its peak set at the 0.25 sigma level. Similar to the observations, the 200-hPa geopotential height and wind responses manifest an atmospheric Rossby wave-like structure. Notably, among three sets of experiments, two prominent centers of anticyclonic circulation anomalies are consistently observed. One is located over North America, around 70°N, and the other is over CA. Additionally, two centers of cyclonic circulation anomalies are evident over the subtropical NA and northern Europe (Fig. 8b, d, and f).

Fast and slow decaying ENSO

Why is the positive phase of the NA SST anomaly pattern stronger in the LC period compared to the HC period? Previous studies have suggested that the surface heat flux anomalies play a dominant role in the formation of the NA horseshoe-like SST anomaly pattern^{4,27–29}. Figure 9 illustrates the regression of JFM(1) latent heat flux and 850-hPa wind with normalized DJF(0) Niño3.4 index in the observations and CMIP6 MME. Here, JFM(1) represents the cross-seasonal months between DJF(0) and MAM(1), which helps in understanding the persistent impacts of anomalous latent heat flux in NA SST anomalies. Compared with the HC period, the anomalous latent

Fig. 6 | Response of 200-hPa geopotential height to North Atlantic SST anomalies. Regression of MAM(1) 200-hPa geopotential height (colors; m) with normalized MAM(1) NAI and the corresponding wave activity flux (vectors; m^2/s^2) in the observation (a) and MME (b). The dots denote the 90% confidence level in the observation and 80% consistency in models.

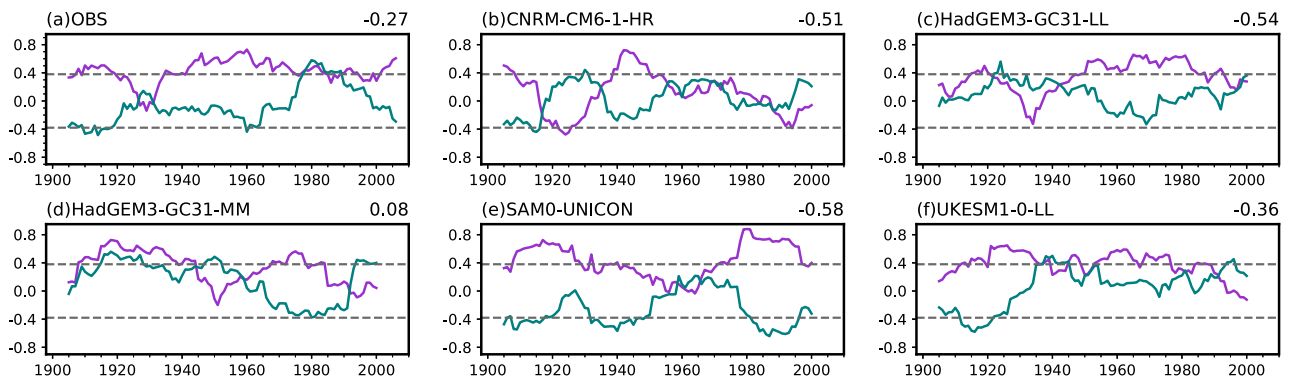
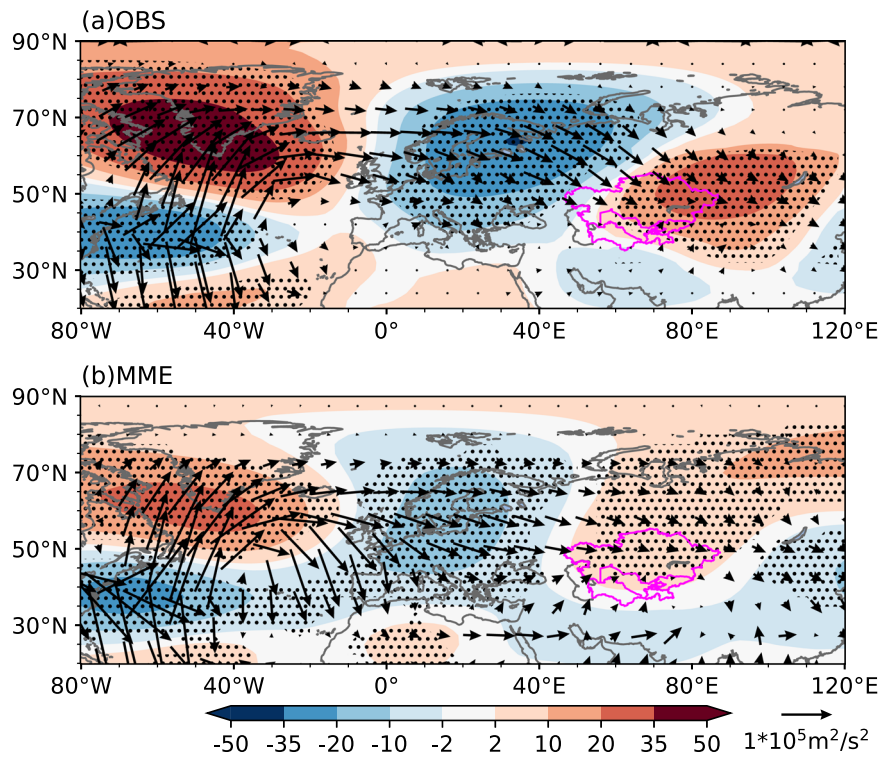


Fig. 7 | Interdecadal relationship of ENSO with SCAP and North Atlantic SST anomalies. The 19-year sliding correlation of MAM(1) precipitation (purple lines; mm/day) over CA and NAI (green lines; K) with normalized DJF(0) Niño3.4 index.

a is for observation and b–f is for five selected models. The numbers at the upper right present the 102-year correlation of the two lines. The gray dashed lines denote the 90% confidence levels of 19-year samples.

heat flux patterns over NA are more pronounced in the LC period. The difference in latent heat flux anomalies between the HC and LC periods could be further attributed to the varying lower-level wind anomalies⁴. Due to the intensified anomalous cyclonic circulation in the mid-latitude NA in the LC period, the stronger southwesterly (northeasterly) anomalies induce a reduction (enhancement) in wind speed and decrease (increase) positive latent heat flux anomalies in the tropical (subtropical) NA. Consequently, it leads to warmer (colder) SST in the tropical (subtropical) NA through wind–evaporation–SST feedback during the LC period compared with the HC period^{30,31}.

Previous studies have indicated that the lower-level wind anomalies over NA in MAM(1) are closely related to ENSO in the tropical eastern Pacific^{20,21}. Therefore, we hypothesize that ENSO may manifest differently in distinct epochs, leading to varying lower-level wind anomalies over NA. We first examine the regressions of DJF(0)

SST with normalized DJF(0) Niño3.4 index in the observations and CMIP6 MME (Supplementary Fig. 5). No significant spatial pattern transitions of ENSO are observed between the HC and LC periods. In the meantime, the observed and MME autocorrelations of the Niño3.4 index with its DJF(0) values display a distinct difference in the ENSO cycle, with observed and MME decaying rates of -0.40 (-0.25) and -0.23 (-0.16) in the HC (LC) period, respectively (Fig. 10a, b). Here, the decaying rate is calculated as the difference between MAM(1) and DJF(0) Niño3.4 index. These quantitative results indicate that the decaying pace of ENSO in the HC period may be faster than that in the LC period. These results are consistent with previous studies, which suggested that the NA horseshoe-like SST anomaly pattern in MAM(1) is stronger and more persistent during the slow than fast decaying ENSO events^{4,32}. The ENSO amplitude is further examined to explore whether it is a potential modulator of the

Fig. 8 | Response of upper-level circulation to vorticity forcing in LBM. **a** Horizontal distribution of imposed atmospheric positive vorticity forcing (colors; $10^{-5} \text{ s}^{-1} \text{ d}^{-1}$) in the North Atlantic. **b** The 200-hPa geopotential height (colors; m) and wind (vectors; m/s) anomalies in response to the vorticity forcing. **c** and **d** same as **a**, **b**, but for negative vorticity forcing. **e** is sum of **a**, **c** and **f** is sum of **b**, **d**.

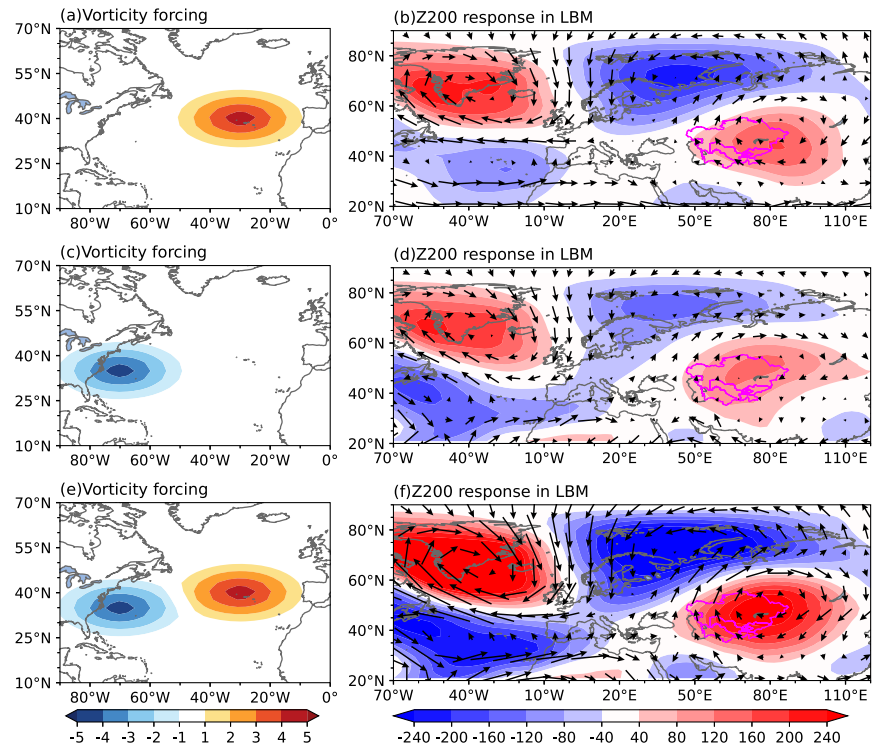
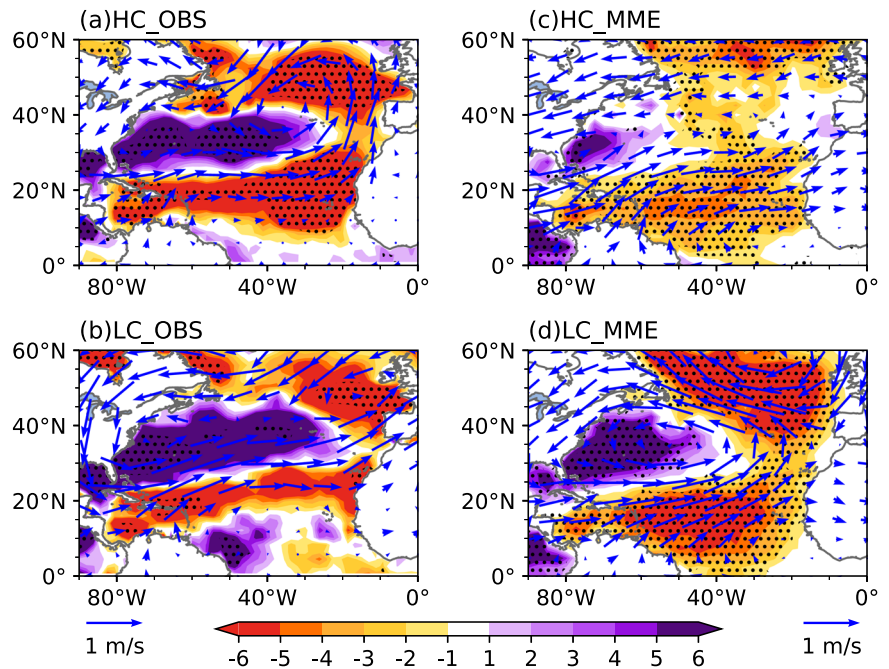


Fig. 9 | Response of latent heat flux and 850-hPa wind to El Niño. Regression of JFM(1) latent heat flux (colors; W/m^2) and 850-hPa wind (vectors; m/s) with normalized DJF(0) Niño3.4 index for **a** HC period and **b** LC period in the observation. **c**, **d** Same as **a**, **b**, but for MME. The dots denote the 90% confidence level in the observation and 80% consistency in models.



ENSO–SCAP relationship. Although stronger ENSO events appear to occur during the observational HC period, there is a lack of consistency among selected CMIP models (Fig. 10c). Furthermore, the 19-year sliding standard deviation of DJF(0) Niño3.4 index, verified across three SST datasets, indicates that the lowest amplitudes of ENSO occur around the 1930s and 1950s, which do not correspond very well with the evolution of ENSO–SCAP (Figs. 1e, 10d). Therefore, the ENSO amplitude may play an important role in the ENSO–SCAP relationship during certain epochs, but it cannot fully explain the historical interdecadal shifts in this relationship. In

conclusion, two distinct types of ENSO decay rates, namely fast and slow decaying ENSO, might be important factors modulating the interdecadal shifts of ENSO–SCAP by influencing the magnitude and phase of the NA SST anomaly pattern.

Driver of ENSO decaying pace

What factors contribute to the variation in the decaying pace of ENSO across different epochs? Previous studies have suggested that the evolution of ENSO may be associated with the decadal variability of the climate system. Figure 11 shows the time series of the

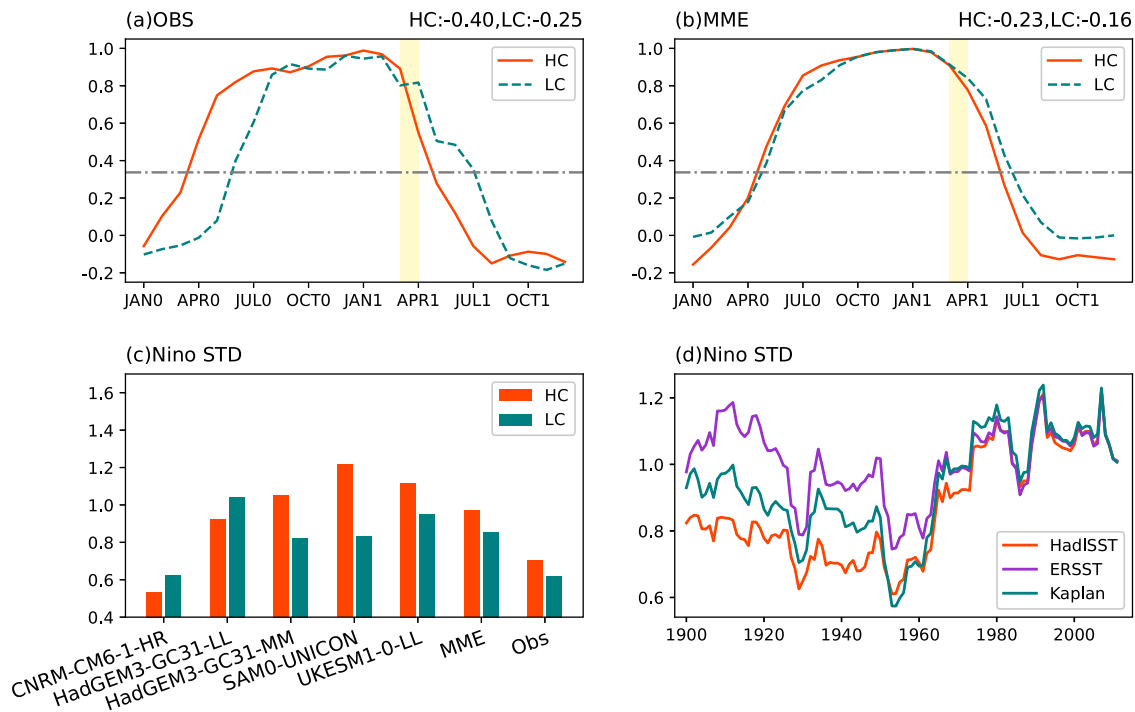


Fig. 10 | Interdecadal variations of ENSO characteristics in observation and selected models. **a** Observed and **b** MME autocorrelation of Niño3.4 index with its DJF(0) values in the HC and LC period. The gray lines denote the 90% confidence level. The light yellow bar indicates the MAM(1) period. The numbers in the upper right corner of panels **a**, **b** are calculated by the seasonal average difference of

Niño3.4 index between MAM(1) and DJF(0). **c** Standard deviation of DJF(0) Niño3.4 index in the HC and LC period for five models, MME, and the observation. **d** The 19-year sliding standard deviation of the Niño3.4 index from HadISST, ERSST and Kaplan SST datasets.

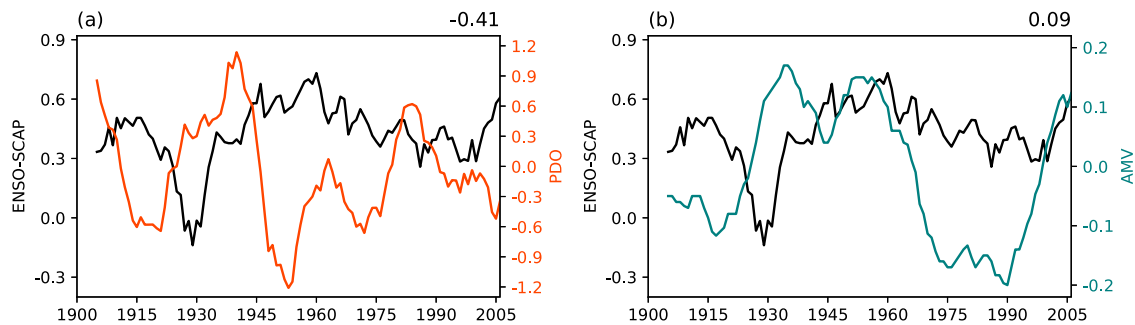


Fig. 11 | Interdecadal shifts in the ENSO–SCAP relationship and its linkage with PDO and AMV. 19-year sliding correlation of the MAM(1) precipitation with the DJF(0) normalized Niño3.4 index (**a**, **b**; black line), 10-year low-pass filtered DJF(0) PDO (**a**; orange line) and AMV (**b**; green line) index in the observation.

ENSO–SCAP relationship, Pacific Decadal Oscillation (PDO) index, and Atlantic Multidecadal Variability (AMV) index in the observations. The results indicate a relatively strong (weak) correlation between PDO (AMV) and ENSO–SCAP, with a correlation coefficient of -0.41 (0.09). To explore the reasons behind the generally strong negative correlation between PDO and ENSO–SCAP, we select El Niño cases during the positive and negative phases of PDO from observations and conduct composite analyses of El Niño-related SST anomalies from DJF(0) to JJA(1). It is found that the positive phase of PDO could lead to slower El Niño decay compared to its negative phase (Supplementary Fig. 6). Regarding the mechanisms, previous research suggests that the positive phase of PDO can enhance trade winds in the tropical Pacific and promote eastward wind convergence. The mean-state changes in tropical winds can induce an eastward displacement of El Niño-related equatorial westerly anomalies, resulting in a prolonged El Niño lifetime³³. As a result, the phase of PDO could modulate the decaying pace of ENSO across different epochs. From this perspective, the strengthening

ENSO–SCAP relationship after the 2000s may be attributed to the negative PDO phase in the recent decade, as this cold phase will favor faster El Niño decay and weaken the positive phase of the NA SST anomaly pattern.

Discussion

The present study investigates interdecadal shifts in the relationship between previous winter ENSO and subsequent SCAP based on observations and CMIP6 simulations. The observed ENSO–SCAP relationship displays pronounced interdecadal shifts, with a sharp decline in the 1930s followed by gradual strengthening around the 1960s. Furthermore, there is an increasing trend after the 2000s.

Two factors may contribute to the interdecadal shifts in the ENSO–SCAP relationship, which is summarized by a schematic diagram in Fig. 12. One factor is changes in the meridional pathway, i.e., large-scale convergence and divergence, through which Pacific SST anomalies influence moisture and dynamical conditions over CA. During warm ENSO events, persistent anomalous upper-level divergence generally prevails over the

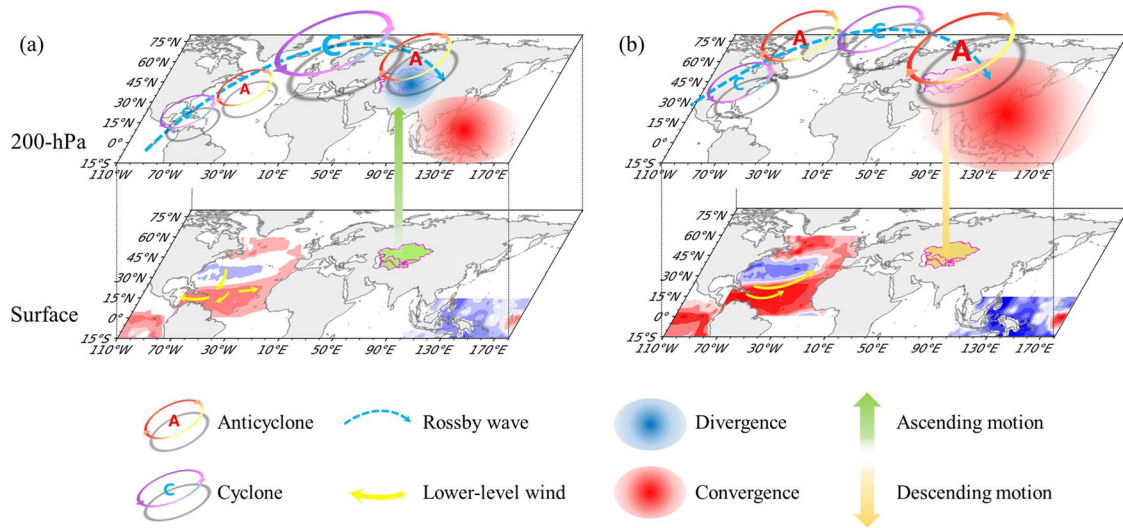


Fig. 12 | Schematic diagram illustrating underlying mechanisms of interdecadal shifts in the ENSO–SCAP relationship. The diagram includes decaying SST anomalies over the tropical Pacific, the NA SST anomaly pattern, precipitation anomalies over CA and the 200-hPa Rossby wave train induced by the NA SST anomaly pattern. **a** is for fast-decaying ENSO epochs and **b** is for slow-decaying ENSO epochs. Red (blue) shadings indicate positive (negative) SST anomalies at the surface and upper-level convergence (divergence) anomalies at 200-hPa,

respectively. The blue dashed curve indicates the Rossby wave train path, and the size of the circles along the curve represents the amplitude of the circulation. The letter A (C) indicates atmospheric anticyclone (cyclone) anomalies. Surface yellow arrows over NA indicate lower-level wind anomalies. Green (brown) shadings and vertical arrows over CA denote above (below) normal precipitation and anomalous ascending (descending) anomalies, respectively.

central-eastern Pacific, while upper-level convergence anomalies emerge over the western Pacific. The large-scale upper-level convergence over the western Pacific further induces upper-level divergence in CA, resulting in anomalous vertical motion and increased local precipitation. The stronger upper-level divergence over CA during the HC period could induce a more robust ascending motion, further contributing to increased precipitation compared to the LC period. The other factor is the changes in the zonal Rossby wave train triggered by NA horseshoe-like SST anomalies. The MAM(1) cold SST anomalies are seen in the middle NA, and warm SST anomalies exist in the NA subpolar gyre zone and tropical NA, which is more pronounced during the LC period than the HC period. This NA SST anomaly pattern plays an opposing role compared to the wetting impacts of El Niño on SCAP, thereby disrupting the ENSO–SCAP relationship. The disruption caused by the NA SST anomaly pattern is more pronounced during the LC period than the HC period, resulting in a stronger ENSO–SCAP relationship in the latter period. We verify the dynamical processes induced by the NA SST anomaly pattern using the LBM. The results align well with our proposed mechanisms, with almost identical Eurasian Rossby wave trains as in the observations.

During the LC period, the stronger anomalous southwesterlies (northeasterlies) in the tropical (subtropical) NA aid in decreasing (increasing) latent heat flux anomalies, heating (cooling) the local SST and resulting in a more pronounced horseshoe-like SST anomaly pattern. Interestingly, the decaying pace of ENSO may modulate the interdecadal shifts of the NA horseshoe-like SST anomaly pattern, which can be further traced back to the phase of PDO. During the positive PDO phase, a slow decaying ENSO triggers a robust NA horseshoe-like SST anomaly pattern during MAM(1), counteracting the impact of ENSO on SCAP. In contrast, during the negative PDO phase, this counteracting effect is weakened, resulting in a more robust ENSO–SCAP relationship.

The findings of this study address important issues concerning the unstable ENSO–SCAP relationship and underlying mechanisms. Moreover, we identify a strengthening tendency in the ENSO–SCAP relationship after the 2000s, which indicates enhanced predictability for SCAP during recent decades. In this sense, this research may offer valuable information for regional stakeholders engaged in seasonal forecasting and climate prediction in arid CA. It should be noted that the NA horseshoe-like SST anomaly pattern is one of the pathways that may interfere with ENSO’s

impact on SCAP. Further research might be necessary to explore additional potential influence factors. Moreover, the factors modulating the decaying pace of ENSO are complex and cannot be solely attributed to PDO. Various influences and mechanisms involved are still unclear and call for future investigations to gain a comprehensive understanding. Furthermore, future efforts are preferred to examine how the ENSO–SCAP relationship will respond to greenhouse warming through projections driven by historical and future radiative forcing imply a slower decay of El Niño in the 21st century³⁴.

Methods

Data

Three datasets of monthly precipitation and three datasets of monthly SST have been used to ensure the reliability of results in the present study. The monthly precipitation datasets include Global Precipitation Climatology Centre (GPCC) monthly product version 2022³⁵, the Climatic Research Unit (CRU) high-resolution gridded datasets version 4.04³⁶, and the University of Delaware (Udel) Air Temperature & Precipitation version v4.01³⁷. In terms of SST datasets, they are sourced from Hadley Centre Sea Ice and SST dataset (HadISST)³⁸, Extended Reconstructed Sea Surface Temperature (ERSST) v5³⁹, and Kaplan Extended SST V2⁴⁰. Global atmospheric circulation data are derived from the NOAA-CIRES-DOE Twentieth Century Reanalysis (20CR) project, Version V2⁴¹. Outputs from the historical experiments of 45 CMIP6 climate models (more details in Supplementary Table 1) are also used. Here, we examine the first ensemble member (normally “r1i1p1f1”) of each model’s historical simulations, which involve running climate models to replicate past climate conditions from 1850 to 2014. These simulations can provide an extensive set of samples to understand the factors driving historical climate variability. Prior to analysis, all the observations and model simulations are bilinearly interpolated onto $2.5^\circ \times 2.5^\circ$ grids in a horizontal manner for uniformity.

Interdecadal shifts

Throughout this study, we focus on the interdecadal shifts of ENSO–SCAP relationship. The 11-year sliding average has been moved from raw data before correlation and regression analysis to remove decadal and longer timescale variations. For a 19-year time series, correlations of 0.39 and 0.46 reach the 90% and 95% confidence levels, respectively, based on the two-sided Student’s *t*-test.

ENSO index

To extract the year-to-year variations of ENSO and monitor the ENSO–SCAP relationship, we define the DJF(0) Niño3.4 index as the areal average of preceding December to following February seasonal mean SST anomalies in the NINO3.4 regions (170°W–120°W, 5°S–5°N). Here, the numbers in parentheses denote ENSO developing (0) and decaying (1) years. The regression of climate anomalies against DJF(0) Niño3.4 index is considered indicative of ENSO-induced climate anomalies. Since the regression analysis is linear, it can demonstrate climate anomalies induced by both El Niño and La Niña events. For simplicity, we primarily show the climate anomalies over CA during post-El Niño springs in the main text.

NA dipole SST index

Considering the potential influence of NA SST anomalies on the ENSO–SCAP relationship, we establish the NA dipole SST index (NAI) for the period MAM(1). This index is computed as the difference between the area-weighted averaged SST anomalies over northeastern region (35°N–55°N, 20°W–40°W) and southwestern region (30°N–50°N, 50°W–80°W), as delineated by the blue and red boxes in Fig. 5c and f, respectively.

Wave-activity fluxes

The horizontal wave-activity fluxes are defined as⁴²

$$W = \frac{1}{2|\vec{V}|} \begin{cases} \bar{U}(\psi_x'^2 - \psi'\psi_{xx}') + \bar{V}(\psi_x'\psi_y' - \psi'\psi_{xy}') \\ \bar{U}(\psi_x'\psi_y' - \psi'\psi_{xy}') + \bar{V}(\psi_y'^2 - \psi'\psi_{yy}') \end{cases} \quad (1)$$

where \vec{V} represents the horizontal wind velocity vector, U and V denote the zonal and meridional wind velocity, respectively. ψ symbolizes the stream function. The primes and overbars signify the regressed anomalies onto the normalized DJF(0) Niño3.4 index and climatological mean-state quantities, respectively.

PDO index

The Pacific decadal oscillation (PDO) is obtained by the leading pattern via empirical orthogonal function analysis of SST anomalies in the North Pacific basin (poleward of 20°N). The SST anomalies are obtained by removing both the climatological annual cycle and the global-mean SST anomaly from the data at each grid point.

AMV index

The Atlantic multidecadal variability (AMV) index is defined as detrended 10-year low-pass filtered DJF(0) mean area-averaged SST anomalies over the North Atlantic basin (0°–65°N, 80°W–0°).

Numerical simulation

In the present study, we employ the dry version of the linear baroclinic model (LBM) to investigate how the atmosphere responds to the vorticity perturbation induced by Atlantic SST anomalies⁴³. The LBM is a model made up of atmospheric primitive equations linearized at a given state. The model has a horizontal resolution of T42 and a vertical resolution of 20σ . We set a maximum e-folding decay time of 6 h for horizontal diffusion to maintain model stability. For different levels of σ , we apply Rayleigh friction and Newtonian damping timescales ranging from 1 to 30 day⁻¹. Vertical diffusion across all layers is fixed at 1000 day⁻¹. We run the model for 50 days to reach a stable state and use the average of the last 30 days as results.

Data availability

All the data that support the findings in the present study are available for open access. The monthly precipitation datasets, including GPCC, CRU, and Udel are accessed from https://opendata.dwd.de/climate_environment/GPCC, https://crudata.uea.ac.uk/cru/data/hrg/cru_ts_4.07 and <https://downloads.psl.noaa.gov/Datasets/udel.airt.precip>, respectively. The HadISST, ERSST, and Kaplan SST datasets

are from <https://www.metoffice.gov.uk/hadobs/hadisst>, <https://www1.ncdc.noaa.gov/pub/data/cmb/ersst/v5/netcdf> and https://psl.noaa.gov/data/gridded/data.kaplan_sst.html, respectively. Global atmospheric circulation dataset is derived from https://psl.noaa.gov/thredds/catalog/Datasets/20thC_ReanV2/Monthlies/gaussian/monolevel/catalog.html. In addition, CMIP6 model outputs are from <https://aims2.llnl.gov/search/cmip6>.

Code availability

All the codes for analyses and diagnostics are available from the corresponding authors upon reasonable request.

Received: 26 March 2024; Accepted: 11 August 2024;

Published online: 23 August 2024

References

- Chen, X., Wang, S., Hu, Z., Zhou, Q. & Hu, Q. Spatiotemporal characteristics of seasonal precipitation and their relationships with ENSO in Central Asia during 1901–2013. *J. Geogr. Sci.* **28**, 1341–1368 (2018).
- Chen, F., Huang, W., Jin, L., Chen, J. & Wang, J. Spatiotemporal precipitation variations in the arid Central Asia in the context of global warming. *Sci. China Earth Sci.* **54**, 1812–1821 (2011).
- Hu, K. et al. Interdecadal variations in ENSO influences on Northwest Pacific–East Asian early summertime climate simulated in CMIP5 models. *J. Clim.* **27**, 5982–5998 (2014).
- Wu, R., Lin, M. & Sun, H. Impacts of different types of El Niño and La Niña on northern tropical Atlantic sea surface temperature. *Clim. Dyn.* **54**, 4147–4167 (2020).
- Yao, J. et al. Intensification of extreme precipitation in arid Central Asia. *J. Hydrol.* **598**, 125760 (2021).
- Hu, Z.-Y. et al. Variations and changes of annual precipitation in Central Asia over the last century. *Int. J. Climatol.* **37**, 157–170 (2017).
- de Beurs, K. M., Henebry, G. M., Owsley, B. C. & Sokolik, I. N. Large scale climate oscillation impacts on temperature, precipitation and land surface phenology in Central Asia. *Environ. Res. Lett.* **13**, 065018 (2018).
- Feng, F., Zhao, Y., Huang, A., Li, Y. & Zhou, X. Different seasonal precipitation anomaly patterns in Central Asia associated with two types of El Niño during 1891–2016. *Front. Earth Sci.* **10**, 771362 (2022).
- Mariotti & Annarita How ENSO impacts precipitation in southwest central Asia. *Geophys. Res. Lett.* **34**, 370–381 (2007).
- Arpe, K. et al. Connection between Caspian Sea level variability and ENSO. *Geophys. Res. Lett.* **27**, 2693–2696 (2000).
- Hurrell, J. W. Influence of variations in extratropical wintertime teleconnections on Northern Hemisphere temperature. *Geophys. Res. Lett.* **23**, 665–668 (1996).
- Zhang, X., He, M., Bai, M. & Ge, Q. Meteorological drought and its large-scale climate patterns in each season in Central Asia from 1901 to 2015. *Clim. Change* **166**, 41 (2021).
- Chen, Z., Wu, R., Zhao, Y. & Wang, Z. Different responses of Central Asian precipitation to strong and weak El Niño events. *J. Clim.* **35**, 1497–1514 (2022).
- Wu, R. et al. Northeast China summer temperature and North Atlantic SST. *J. Geophys. Res. Atmos.* **116**, D16116 (2011).
- Chen, S., Wu, R., Chen, W., Hu, K. & Yu, B. Structure and dynamics of a springtime atmospheric wave train over the North Atlantic and Eurasia. *Clim. Dyn.* **54**, 5111–5126 (2020).
- Ma, Q. et al. How do multiscale interactions affect extreme precipitation in eastern Central Asia? *J. Clim.* **34**, 7475–7491 (2021).
- Umirbekov, A., Peña-Guerrero, M. D. & Müller, D. Regionalization of climate teleconnections across Central Asian mountains improves the predictability of seasonal precipitation. *Environ. Res. Lett.* **17**, 055002 (2022).

18. Vicente-Serrano, S. M. et al. The Westerly Index as complementary indicator of the North Atlantic oscillation in explaining drought variability across Europe. *Clim. Dyn.* **47**, 845–863 (2016).
19. Xu, G. et al. Regional drought shifts (1710–2010) in East Central Asia and linkages with atmospheric circulation recorded in tree-ring $\delta^{18}\text{O}$. *Clim. Dyn.* **52**, 713–727 (2019).
20. Alexander, M. A. et al. The Atmospheric Bridge: the influence of ENSO teleconnections on air–sea interaction over the global oceans. *J. Clim.* **15**, 2205–2231 (2002).
21. Klein, S. A., Soden, B. J. & Lau, N.-C. Remote sea surface temperature variations during ENSO: evidence for a tropical atmospheric bridge. *J. Clim.* **12**, 917–932 (1999).
22. Rana, S., McGregor, J. & Renwick, J. Dominant modes of winter precipitation variability over Central Southwest Asia and inter-decadal change in the ENSO teleconnection. *Clim. Dyn.* **53**, 5689–5707 (2019).
23. Hoell, A. et al. The forcing of monthly precipitation variability over Southwest Asia during the Boreal Cold Season. *J. Clim.* **28**, 7038–7056 (2015).
24. Hoell, A., Barlow, M. & Saini, R. Intraseasonal and seasonal-to-interannual Indian Ocean convection and hemispheric teleconnections. *J. Clim.* **26**, 8850–8867 (2013).
25. Zhang, Y. & Wu, R. Asian meteorological droughts on three time scales and different roles of sea surface temperature and soil moisture. *Int. J. Climatol.* **41**, 6047–6064 (2021).
26. Zhang, J. et al. Influences of tropical Pacific and North Atlantic SST anomalies on summer drought over Asia. *Clim. Dyn.* **61**, 5827–5844 (2023).
27. Huang, B. & Shukla, J. Ocean–atmosphere interactions in the tropical and subtropical Atlantic Ocean. *J. Clim.* **18**, 1652–1672 (2005).
28. Enfield, D. B. & Mayer, D. A. Tropical Atlantic sea surface temperature variability and its relation to El Niño–Southern Oscillation. *J. Geophys. Res. Oceans* **102**, 929–945 (1997).
29. Curtis, S. & Hastenrath, S. Forcing of anomalous sea surface temperature evolution in the tropical Atlantic during Pacific warm events. *J. Geophys. Res. Oceans* **100**, 15835–15847 (1995).
30. Xie, S. The shape of continents, air–sea interaction, and the rising branch of the Hadley circulation (2004).
31. Xie, S. A dynamic ocean–atmosphere model of the tropical Atlantic decadal variability. *J. Clim.* **12**, 64–70 (1999).
32. Lee, S. K., Enfield, D. B. & Wang, C. Why do some El Niños have no impact on tropical North Atlantic SST?. *Geophys. Res. Lett.* **35**, L16705 (2008).
33. Feng, J., Wang, L. & Chen, W. How does the East Asian summer monsoon behave in the decaying phase of El Niño during different PDO phases? *J. Clim.* **27**, 2682–2698 (2014).
34. Lopez, H., Lee, S.-K., Kim, D., Wittenberg, A. T. & Yeh, S.-W. Projections of faster onset and slower decay of El Niño in the 21st century. *Nat. Commun.* **13**, 1915 (2022).
35. Schneider, U., Hänsel, S., Finger, P., Rustemeier, E. & Ziese, M. *GPCC Full Data Monthly Product Version 2022 at 0.5°: Monthly Land–surface Precipitation from Rain-gauges Built on GTS-based and Historical Data [Data set]* (Global Precipitation Climatology Centre (GPCC), 2022).
36. Harris, I., Osborn, T. J., Jones, P. & Lister, D. Version 4 of the CRU TS monthly high-resolution gridded multivariate climate dataset. *Sci. Data* **7**, 109 (2020).
37. Matsuura, K. & Willmott, C. *Terrestrial Air Temperature: 1900–2008 Gridded Monthly Time Series (Version 4.01)* (Department of Geography Center, University of Delaware, 2015).
38. Rayner, N. et al. Global analyses of sea surface temperature, sea ice, and night marine air temperature since the late nineteenth century. *J. Geophys. Res. Atmos.* **108**, 4407 (2003).
39. Huang, B. et al. Extended reconstructed sea surface temperature, version 5 (ERSSTv5): upgrades, validations, and intercomparisons. *J. Clim.* **30**, 8179–8205 (2017).
40. Kaplan, A. et al. Analyses of global sea surface temperature 1856–1991. *J. Geophys. Res. Oceans* **103**, 18567–18589 (1998).
41. Schneider, D. P., Deser, C., Fasullo, J. & Trenberth, K. E. Climate data guide spurs discovery and understanding. *EOS Trans. Am. Geophys. Union* **94**, 121–122 (2013).
42. Takaya, K. & Nakamura, H. A formulation of a phase-independent wave-activity flux for stationary and migratory quasigeostrophic eddies on a zonally varying basic flow. *J. Atmos. Sci.* **58**, 608–627 (2001).
43. Watanabe, M. & Kimoto, M. Atmosphere–ocean thermal coupling in the North Atlantic: a positive feedback. *Q. J. R. Meteorol. Soc.* **126**, 3343–3369 (2000).

Acknowledgements

We thank the anonymous reviewers for their constructive comments and suggestions, which significantly enhances the quality of the manuscript. We acknowledge the World Climate Research Program (WCRP)'s Working Group on Coupled Modeling, and we extend our gratitude to the climate modeling groups worldwide (listed in Supplementary Table 1) for their efforts in producing and making their model outputs publicly available. This work was funded by the National Natural Science Foundation of China (42141019 and 42261144687).

Author contributions

M.Y.: Investigation, data curation, formal analysis, drafting the manuscript, writing review, and editing. H.T.: Conceptualization, methodology, formal analysis, writing review, and editing. G.H.: Supervision, funding acquisition, project administration, writing review, and editing. R.W.: Formal analysis, writing review, and editing. All authors have read and approved the final manuscript.

Competing interests

The authors declare no competing interests.

Additional information

Supplementary information The online version contains supplementary material available at <https://doi.org/10.1038/s41612-024-00742-x>.

Correspondence and requests for materials should be addressed to Haosu Tang or Gang Huang.

Reprints and permissions information is available at <http://www.nature.com/reprints>

Publisher's note Springer Nature remains neutral with regard to jurisdictional claims in published maps and institutional affiliations.

Open Access This article is licensed under a Creative Commons Attribution-NonCommercial-NoDerivatives 4.0 International License, which permits any non-commercial use, sharing, distribution and reproduction in any medium or format, as long as you give appropriate credit to the original author(s) and the source, provide a link to the Creative Commons licence, and indicate if you modified the licensed material. You do not have permission under this licence to share adapted material derived from this article or parts of it. The images or other third party material in this article are included in the article's Creative Commons licence, unless indicated otherwise in a credit line to the material. If material is not included in the article's Creative Commons licence and your intended use is not permitted by statutory regulation or exceeds the permitted use, you will need to obtain permission directly from the copyright holder. To view a copy of this licence, visit <http://creativecommons.org/licenses/by-nc-nd/4.0/>.

© The Author(s) 2024